Analytica Chimica Acta 1195 (2022) 339455

Contents lists available at ScienceDirect

Analytica Chimica Acta

journal homepage: www.elsevier.com/locate/aca

Monitoring of viral myocarditis injury using an energy-confined upconversion nanoparticle and nature-inspired biochip combined CRISPR/Cas12a-powered biosensor

Li-Li Lu [a], Chao-Zhi Li [a], Heng-Zhong Guo [a], Da Liu [b], Hong-Wu Tang [b], Bei Zheng [c], Cheng-Yu Li [a, *]

[a] Hubei Province Key Laboratory of Occupational Hazard Identification and Control, Medical College, Wuhan University of Science and Technology, Wuhan, 430065, People's Republic of China
[b] College of Chemistry and Molecular Sciences, Wuhan University, Wuhan, 430072, People's Republic of China
[c] Westlake Institute for Advanced Study, School of Life Sciences, Westlake University, Hangzhou, 310024, People's Republic of China

HIGHLIGHTS

- A dual-aptamer-regulated CRISPR/Cas12a system for transducing a protein target is proposed.
- An energy-confined upconversion nanoparticle is incorporated to face with complicated samples.
- A three-dimensional photonic crystal interface-coated biochip is utilized to boost the upconversion luminescence.
- The sensing method can work as an efficient tool for dynamic monitoring viral myocarditis injury.

GRAPHICAL ABSTRACT

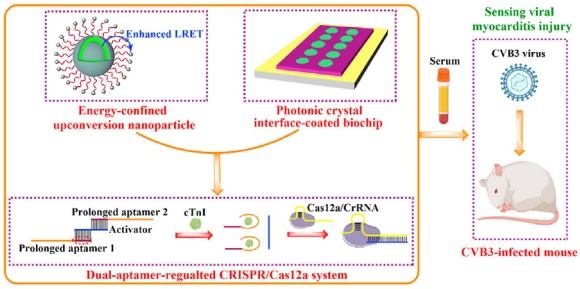

ARTICLE INFO

Article history:
Received 7 December 2021
Received in revised form
4 January 2022
Accepted 5 January 2022
Available online 7 January 2022

Keywords:
Viral myocarditis
Upconversion luminescence
Biochip
CRISPR
Cardiac troponin I

ABSTRACT

The early diagnosis and timely intervention of viral myocarditis urgently require a noninvasive detection approach. Therefore, we present a CRISPR/Cas12a-powered biosensor that integrates an exceptionally efficient upconversion luminescent resonance energy transfer (LRET) with a nature-inspired biochip to determine a golden-standard cardiac biomarker (cardiac troponin I). First, a unique sandwich-structured energy-confined upconversion nanoparticle (acting as the energy donor) is synthesized to dramatically reinforce the LRET's ability. Such a structural improvement endows a relatively high quenching efficiency (as much as 93.8%) toward the surface acceptors and enhances the working adaption in complicated biological media. Moreover, a three-dimensional photonic crystal fabricated using a self-assembly of nanospheres is employed to construct a biochip interface, under which the upconversion luminescence is prominently boosted to approximately 27-fold to achieve signal amplification. Finally, the newly developed luminescence sensing method exhibits remarkable assay performance after introducing these attempts into a dual-aptamer-regulated CRISPR/Cas12a system to transduce the target. More importantly, this biosensor can primarily be a quite useful tracer tool to allow dynamic monitoring of the entire myocardial injury process in a coxsackievirus B3 infected mouse model, paving an attractive venue for medical diagnostic techniques.

* Corresponding author.
URL: http://li-chengyu@wust.edu.cn

https://doi.org/10.1016/j.aca.2022.339455
0003-2670/

1. Introduction

Viral myocarditis is characterized by localized or diffuse inflammatory lesions in myocardium caused by virus infections. It has been regarded as the main pathogenic factor for dilated cardiomyopathy-induced heart failure [1–3]. Clinically, several viruses, including coxsackieviruses [4], adenoviruses [5], parvovirus [6] and herpesvirus [7], have been reported as pathogens that can cause myocardial injuries. These injuries, along with several other severe cases accompanied by a series of full-body sequelae, show no considerable differences in age, ethnicity, and sex [3]. Therefore, viral myocarditis is becoming a serious public health issue (the incidence rate is as high as 20/10,000 people [2]) and developing an effective medical diagnostic technique to ensure timely intervention is an urgent requirement. Thus far, endomyocardial biopsy and cardiac magnetic resonance imaging were the most frequently applied detection methods [1,2]. However, the former is an invasive and challenging operation and the latter can only estimate the patients who appear substantial heart problems. By contrast, cardiac biomarkers are more promising identification targets for early diagnosis and also dynamic monitoring the complete pathological process [8–10]. Cardiac troponin I (cTnI) is currently recognized as the golden-standard marker owing to its universal positive effect [9,10].

Although various biosensors-assisted assay platforms such as luminescence [11,12], colorimetry [13,14], mass spectrometry [15] and electrochemistry [16–18] are successful at sensitively determining cTnI, there is a considerable difficulty in distinctly improving the sensing accuracy. A revolutionary "genetic scissor", the clustered regularly interspaced short palindromic repeats (CRISPR) system, can help in overcoming this challenge. CRISPR is an immune weapon used by bacteria to eliminate viral invasion. It is directionally activated to degrade the exogenous genome by combining a Cas endonuclease family with a guided RNA (denoted as CrRNA). Thus, benefiting from the extremely strict base-pairing-triggered cleavage principle, the further integration of the CRISPR system and some advanced biosensing strategies can promote the precision of target transduction [19–21]. A recently discovered type-V endonuclease, Cas12a, has the traditional cleavage ability (termed as *cis* cleavage) toward a target nucleic acid and an additional indiscriminate cleavage effect (termed as *trans* cleavage) to an arbitrary noncomplementary single-stranded DNA molecule (termed as a reporter) [22,23]. With such a collateral cleavage mechanism, better design flexibility will be obtained when incorporating a stable and simple luminescence output.

The present integration strategies for CRISPR/Cas12a system are still challenging, in the sense that most of the luminescence outputs follow a routine Stokes emission through excitation with a source in the visible wavelength range [24–26]. Thus, the strong background signals such as autoluminescence in complicated biological media (*e.g.* serum) render these sensing reports lacking or adequate in terms of anti-interference [27], particularly for working in low-abundance samples (the background signals may cover the positive results). Owing to this drawback, an ideal choice for a special near-infrared light converting luminescence behavior, known as the upconversion luminescence, is considered [28–31]. Generally, a low-cost and convenient continues wave (CW) laser device is utilized to execute an anti-Stokes pattern to provide a zero-background output. Moreover, the doping nanostructure can offer outstanding resistance to environmental factors. Furthermore, a luminescent resonance energy transfer (LRET) pathway with multiple signals is commonly employed to avoid false optical information by selecting upconversion nanoparticles (UCNPs) as the energy donors [32,33]. Unfortunately, conventional UCNPs own a relatively large size (normally >25 nm), making it difficult for the matched energy acceptors to be within the required optimal spatial distance of LRET (<10 nm); hence, causing a bottleneck in the LRET efficiency reinforcement (commonly <50%) and subsequently affecting sensing performance. Therefore, satisfying such a purpose by exploring a structural alternation to restrict the luminescence domain is necessary.

Apart from strengthening anti-interference ability, seeking a proper sensing interface is vital. This is because the existing luminescent CRISPR/Cas12a-powered biosensors are almost constructed in homogenous solutions; therefore, the deficiency of target enrichment makes the conduction of highly sensitive analysis tedious. However, we can obtain some inspiration from a wealth of array-type structures found in nature [34–38]. For instance, the wings of Morpho butterfly can intensively reflect sunlight owing to the periodic arrangement of their flakes [37]. Based on this hint, several nature-inspired microscopic structures are artificially created to actualize the selective effect of light. Accordingly, a sort of three-dimensional biomimetic interface formed by a random self-assembly phenomenon between nanospheres [typically called photonic crystal (PC)] is considered. These structures have been utilized as an effective auxiliary toolbox to enhance diverse luminescent materials by advoiding the loss of transmitted signals through its photonic band gap [36–38].

To address the aforementioned issues, an exceptionally efficient upconversion LRET and PC interface-coated biochip supporting a CRISPR/Cas12a-powered biosensor under the regulation of dual-aptamer was proposed. This highly integrated biosensor was then applied to dynamically monitor the myocardial injury (determined by the variations in serum cTnI) in a coxsachie virus B3 (CVB3) infected mouse model. The sensing mechanism and the workflow of this artful biosensor are exhibited in Scheme 1. Here, two appropriately prolonged cTnI aptamers and an activator (perfectly complementary to the CrRNA) are annealed to achieve a blocking event. In the presence of cTnI (existing in the serum of CVB3-infected mouse), owing to the stronger affinities to the partially hybridized duplex chains with only 11 nt in the half region (blue line), the completely exposed dual-aptamer (orange lines) will identify the cTnI in priority (demonstrated in Fig. S1). After further releasing the activator to freely combine the Cas12a/CrRNA complex, the CRISPR/Cas12a system is finally activated. Another point, the black hole quencher 1 (BHQ-1) labeled reporter is covalently attached to a peculiar sandwich-structured energy-confined UCNP through the functionalization of the ploy acrylic acid (PAA) polymers on its surface (denoted as SUCNP-PAA). For the reporters attached SUCNP-PAA, the inner shell confined upconversion luminescence will be observably quenched by the proximate BHQ-1 molecules. Upon degrading the activators and reporters by the *cis*- and *trans*-cleavage reactions, respectively, the collaterally cleaved products are loaded onto the biochip to obtain a smartphone-placed above the biochip-based image capturing (which is a good alternative to supply an economical instrument [39–41]) under the irradiation a portable 980-nm CW laser device and the gray level quantifies the final signal.

2. Experimental section

2.1. Oleic acid (OA) stabilized core matrix ($NaYF_4$) synthesis (Core-OA)

A mixed solution (21 mL) prepared by a specific volume proportion of 1-octadecene (1-ODE) and OA (5:2) was magnetically stirred with 1 mmol of $YCl_3 \cdot 6H_2O$ at room temperature in a 100 mL flask (duplex-neck round-bottom). Once the small solids had dissolved, the flask was placed in an electric heating mantle and further vacuum treated through an oil pump until no bubbles were

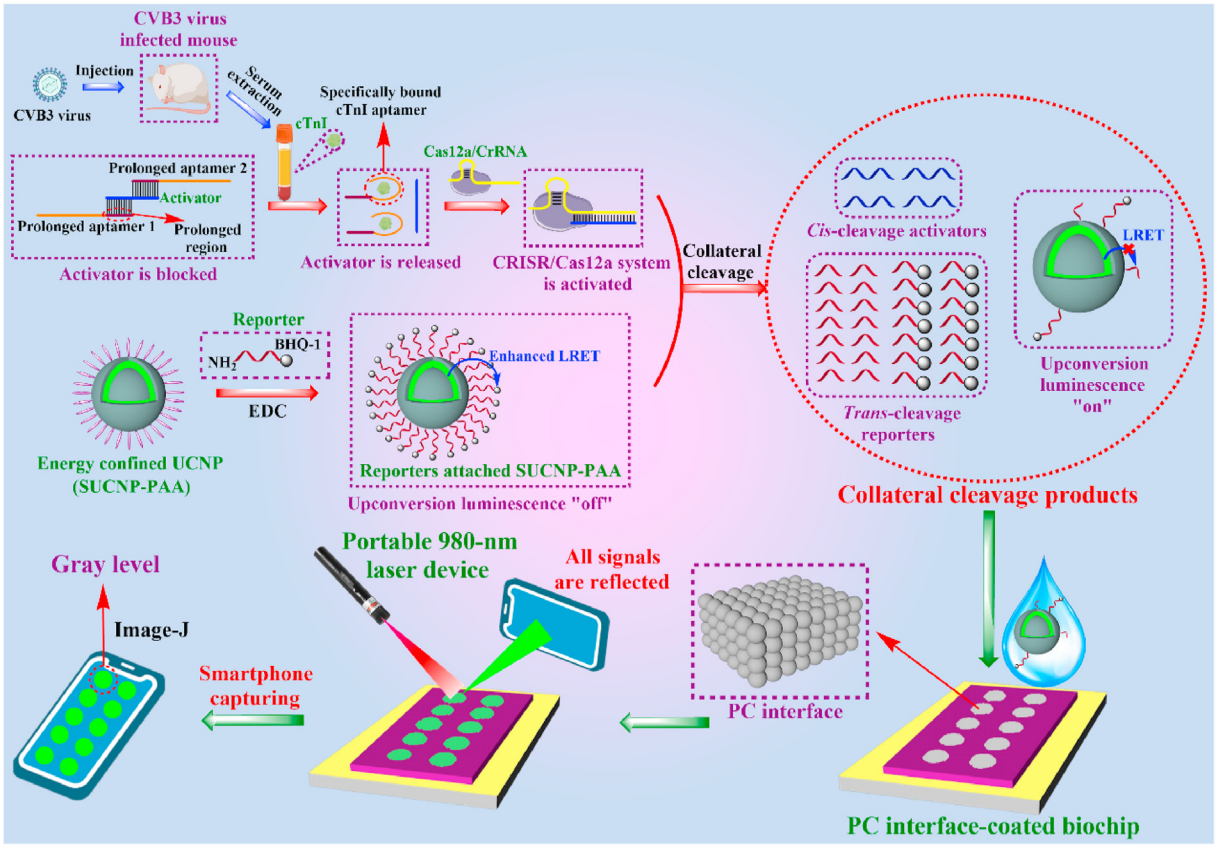

Scheme 1. Sensing mechanism and workflow of exceptionally efficient upconversion LRET, PC interface-coated biochip and dual-aptamer regulation supported CRISPR/Cas12a-powered biosensor for dynamic monitoring of viral myocarditis injury.

present on the liquid surface. Next, the mixture was rapidly heated to 150 °C (heating rate = 15 °C/min) under a high-speed Ar- flow environment, maintaining the warm and intensive stirring for approximately 40 min to dissolve the remaining bulk chlorides completely. This step was followed by cooling the as-obtained clear solution to room temperature. Simultaneously, a drop-by-drop addition of an ultrasound-prepared methanol solution (10 mL), formed from dissolving 4 mmol of NH_4F and 2.5 mmol of NaOH was initiated. After stirring the as-formed oleates gently for another 15 min, the unused methanol, residual oxygen and water were evaporated together by degassing the flask at 120 °C for at least 20 min, followed by increasing the mixture temperature to 300 °C in 25 min. While keeping the Ar-flow protection for another 60 min to turn the white-cloudy solution to a light-yellow transparent liquid, the slightly yellowish products were cooled and precipitated by introducing excess acetone into resulting solution and then employing centrifugation (13,000 rpm for 10 min) for collection. Subsequently, eight-5 mL tubes were used to divide the as-acquired solids evenly. Next, each aliquot was washed several times with a mixture of ultrapure water and ethanol (v/v = 1:1) to collectively remove the unreacted inorganic and organic sources. In addition, the as-washed nanoparticles were purified by a mixture of cyclohexane and ethanol (v/v = 1:8) to disperse the core matrix better. Finally, the concentration of the nanoparticles was regulated at ~20 mg/mL under an ultrasound system for 3 min in 4-mL chloroform solution (forming a homogeneous solution) and stored in a freezer at 4 °C to achieve subsequent inner shell development.

2.2. OA stabilized inner shell matrix ($NaYF_4$: 18% Yb, 2% Er) development (core-shell-OA)

Initially, a 50-mL flask (duplex-neck round-bottom) was provided in turn with a mixture (10.5 mL) of 1-ODE/OA (v/v = 5:2) and 0.25 mmol of lanthanide chlorides (where the specific molar proportion of Y/Yb/Er is 0.8/0.18/0.02). After stirring thoroughly, vacuuming, and heating to 150 °C, a freshly obtained methanol solution (5 mL) containing 2 mmol of NH_4F and 1.25 mmol of NaOH was added to the cooled flask, followed by adding the oleates with 2 mL of the as-synthesized core matrix. After the methanol and chloroform were completely evaporated by degassing at 120 °C, the white-cloudy solution transformed into a transparent liquid. Next, the flask was heated to 300 °C under an Ar-flow environment and cooled to room temperature after keeping it warm for another 30 min. Finally, the products precipitated by adding excess acetone were collected, washed, purified, and stored in a freezer at 4 °C (dispersed into 2 mL of chloroform to regulate their concentrations at ~ 20 mg/mL), enabling the subsequent development of the outer shell.

2.3. OA stabilized outer shell matrix ($NaYF_4$) development (SUCNP-OA)

Here, 0.25 mmol of $YCl_3 \cdot 6H_2O$ was first stirred intensively with a mixture (10.5 mL) of 1-ODE/OA (v/v = 5:2) in a 50 mL flask (duplex-neck round-bottom) and was further vacuumed and heat treated. Subsequently, a methanol mixture (5 mL) containing a certain molar proportion of NH_4F (2 mmol) and NaOH (1.25 mmol) was introduced into the cooled flask to form the white-cloudy

oleates. Afterward, 1 mL of the as-synthesized Core-Shell-OA was added to the sample. The methanol and chloroform were evaporated by degassing and the resulting solution was heated to 300 °C and kept warm for 20 min. The obtained transparent solution was cooled to room temperature and treated with excess acetone to precipitate the light-yellow solids. By centrifuging, collecting, washing, and purifying, the resulting products were dispersed into 2 mL of chloroform (concentration = 20 mg/mL) *via* ultrasound for at least 15 min and stored in a freezer at 4 °C for the subsequent water-soluble functionalization. To control the size of the outer shell matrix, 1-ODE/OA with different volume ratios could be added for this synthetic procedure.

2.4. Preparation of PAA functionalized SUCNP (SUCNP-PAA)

In this case, 25 mL of diethylene glycol was first dissolved with 400 mg of PAA in a 30-mL tube *via* ultrasound treatment until a clear solution was obtained. The mixture was then transferred into a 50-mL flask (three-neck round-bottom). Next, the flask was vacuum treated and further heated to 100 °C under Ar protection and injected with 500 μL of the as-synthesized SUCNP-OA drop by drop. After maintaining a gentle stir for 60 min to thoroughly remove the unused chloroform, the mixture was quickly heated to a temperature of 220 °C. After keeping this warm for another 180 min, the resulting products were precipitated through the addition of excess acetone and high-speed centrifugation (20,000 rpm for 10 min) was then used to collect the white solids. Finally, 1 mL of ultrapure water was used to disperse the final water-soluble nanoparticles (concentration = 10 mg/mL) by washing them three times with ethanol and stored in a freezer at 4 °C for a long-period.

2.5. Covalent attachment between reporter and SUCNP-PAA

First, 10 μL of 10-μM reporter (dissolved into ultrapure water) was thoroughly mixed with 10 μL of the as-prepared SUCNP-PAA in a 1.5 mL-tube *via* ultrasound for 2 min. The mixture was then supplied with a 100 μL of 2-Morpholinoethanesulfonic (MES) acid buffer solution (10 mM, pH 6.5) and a 10 μL of 5 mg/mL freshly-prepared 1-ethyl-3-(3-dimethylamino-propyl)carbodiimide hydrochloride (EDC) solution (prepared using MES buffer solution), and transferred to a 37 °C gas-type oscillator to perform a gentle incubation for 30 min. Afterward, a small quantity of highly concentrated (50 mg/mL) EDC solution was introduced into the tube to facilitate the attachment process. Then, gently incubating for another 90 min, the unattached reporters were removed by centrifuging the mixture at 10,000 rpm for 10 min. The final products were re-dispersed into a 100 μL of Tris (hydroxymethyl) methyl aminomethane reaction buffer solution (30 mM, 0.2 mg/mL bovine serum albumin, 15 mM $MgCl_2$, and pH 8.0) through a vortex.

2.6. Fabrication of PC interface-coated biochip

Before this experiment, a 0.17-mm-thick of cover glass (length: 50 mm, width: 22 mm) should be thoroughly soaked in 5% hydrochloric acid, mixture of acetone/ethanol (v/v = 2:3), and ultrapure water under ultrasound treatment (each step was maintained for 20 min). Next, Ar-flow was used to blow-dry the residual liquids on the as-cleaned glass surface. Then, the cover glass was placed in a 90-mm watch glass, which was added with 18 mL of aminopropyltriethoxysilane (APTES) and continued the immersion process for 10 h. After coating the as-silanized cover glass with a thin layer (~4 mm) of polydimethylsiloxane (PDMS) interface in a 60 °C vacuum environment achieved by a dust-free oven, ten round holes with a diameter of 5 mm were punched onto the as-prepared PDMS layer at equal intervals. This was followed by carefully dropping into each hole 20 μL of droplets containing ultrapure water dispersed 240 nm carboxyl polystyrene spheres (CPSs, concentration = 50 mg/mL). After the droplet-loaded cover glass was held at a 37 °C oven for about 120 min, the final PC interface-coated biochip was cleaned again through Ar-flow and further put into a glass desiccator at room temperature for long-period storage.

3. Results and discussion

3.1. Preparation route, progressive characterization, and surface modification/attachment of sandwich-structured energy-confined UCNP

As illustrated in Fig. 1A, each OA-stabilized hydrophobic layer of the unique sandwich-type UCNP is prepared by adopting an environmental-friendly (using chloride precursors) thermal decomposition synthetic strategy-based seed-growth approach [42]. In brief, a $NaYF_4$ seed is first prepared at a high temperature (300 °C) to serve as the core matrix. Then, a very thin (~2 nm) co-doped $NaYF_4$ inner shell matrix is developed onto the core surface (denoted as $NaYF_4$@ $NaYF_4$, Yb, Er) to act as the luminescence layer, by which a classical activator-to-sensitizer energy transfer between 18% Yb^{3+} and 2% Er^{3+} is confined in such extremely narrow spatial distance. Next, a $NaYF_4$ outer shell matrix needs to be extended onto this core-shell structure (denoted as $NaYF_4$@ $NaYF_4$, Yb, Er@$NaYF_4$) to further prevent the limited luminescence domain from solvent quenching. In order to achieve the follow-up biomolecular attachment through a covalent method, a facilitated ligand exchange mechanism (220 °C at the liquid-liquid interface) is performed by employing PAA with low molecular weight (MW = 1800 Da) to the aforementioned layer-by-layer mediation case, instead of the original OA capping.

Consecutive transmission electron microscopy (TEM) images shown in Fig. 1B–D reveal the specific morphological evolution of this crystal-broadening treatment, wherein spherical shapes with outstanding monodispersities (with no agglomeration) are assigned to all the matrix developments. No changes in morphology and dispersion features are observed for the emergence of the new hydrophilic ligand (Fig. 1E). Further statistical results (n = 200, Figs. S2A–S2D) indicate that the size distribution of all the nanostructures fall in a very narrow range [the value of relative standard deviations (RSDs) are at approximately 6%], with exact average particle diameters of 25.55, 27.72, and 30.04 nm for Core-OA, Core-Shell-OA (corresponding to an inner shell of 2.17 nm) and SUCNP-OA (corresponding to an outer shell of 2.32 nm), respectively, together with negligible fluctuations occurring in the SUCNP-PAA (29.93 nm). Moreover, large areas of crystallization (high-resolution TEM images in Figs. S3A–S3D) are well maintained for this size increment process, among which the adjacent intercepts of these single-crystal space fringes are measured as approximately 5.2 Å, an evident indication of the formation of (100) lattice plane during the layer growth. Such hexagonal-like crystal properties are collectively confirmed by the X-ray diffraction (XRD) phase analyses (Fig. 1F), wherein all the characteristic positions of diffraction peaks (no impurities are present) are found to be ideally in consistent with the standard pattern (JCPDs: 28–1192) of pure β-$NaYF_4$, demonstrating the lattice integrities of the as-proposed preparation route. Energy-dispersive X-ray spectroscopy (EDX) is employed to determine the concrete metal mappings of these nanomaterials (Fig. 1G), where it is apparent that the surface of Core-Shell-OA is surrounded by a ring of Yb and Er, suggesting that the inner shell can perfectly confine the emitters. Accompanied by the emergence of some typical transmittance bands (three bottom lines in Fig. 1H) in the Fourier-transform infrared (FT-IR) spectra for OA molecules, i.e.,

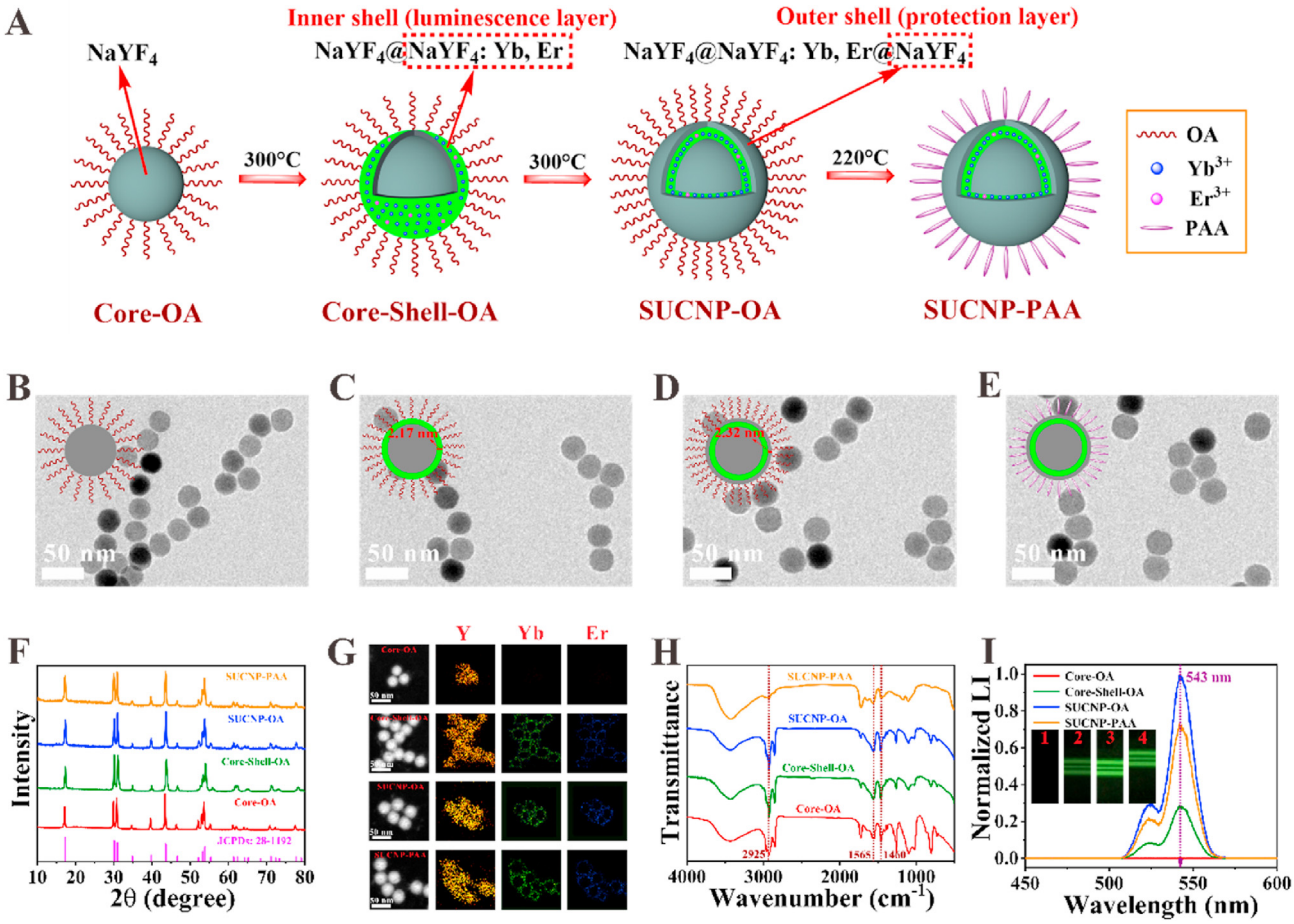

Fig. 1. (A) Preparation route of sandwich-structured energy-confined UCNP and its surface modifications. (B)–(E) TEM images of Core-OA, Core-Shell-OA (inner shell development), SUCNP-OA (outer shell development) and SUCNP-PAA (hydrophilic functionalization). Scale bars are 50 nm. (F)–(I) XRD phase analyzes, metal mappings, FI-IR spectra and upconversion luminescence spectra of these nanostructures. Insets in (I): real digital images of these nanoparticles dispersed into corresponding solvents (1–3 in chloroforms and 4 in ultrapure water).

the symmetric (1565 cm^{-1}) and the antisymmetric (1460 cm^{-1}) vibrations of $RCOO^-$ as well as the stretching (2925 cm^{-1}) of the asymmetrical long alkyl chain, the expected hydrophobic modification is effectively confirmed. The referred nonpolar surfaces ensure favorable dispersion abilities in the chloroform (Figs. S4A–S4C). Comparatively, an apparent attenuation tendency occurred in the functionalization of PAA polymers (top line in Fig. 1H), which resulted in a homogenous solution after re-dispersing into ultrapure water (Fig. S4D).

Upon irradiating these transparent solutions with a 980-nm CW laser device (laser power ~ 1 W), the introduction of the outer shell can act as a natural protective barrier to efficiently restrain the interaction of solvent molecules to the luminescence layer. Therefore, the green emissions of corresponding digital images are markedly enhanced (insets 1–3 in Fig. 1I). Furthermore, compared to the presence of the completely bared luminescence, such enhancement effect is accurately assessed by upconversion luminescence spectra (green and blue lines in Fig. 1I), in which the maximal emission wavelength located around 543 nm deriving from the energy-level transition (Fig. S5, from $^4S_{3/2}$ to $^4I_{15/2}$) of Er^{3+} is boosted to about four times. Although the inevitable non-radiative relaxation [43] compels the featured luminescence of the water-soluble case to drop by ~ 25% (orange line and inset 4 in Fig. 1I), the stabilities of colloid and optics are flawlessly retained for as long as 30 days of storage (Fig. S6), resulting in a good luminescence output and a powerful nanocarrier for realizing the forthcoming biomolecule binding.

When the reporter attachment event is conducted using the EDC-activated covalent coupling reaction, the original negative potential (−21.5 mV, owing to the presence of carboxyl groups) of SUCNP-PAA further decrease in negative (−27.8 mV, Fig. S7A), which can be attributed to the negative charge of DNA molecules and a slight increase (thickened by approximately 1.3 nm, Fig. S7B) occurs to the hydrate particle sizes. Apart from these findings, the complete disappearance of ultraviolet absorption at 260 nm (originating from various conjugated systems of nucleic acids [44]) in the collected reaction supernatant confirms a highly efficient surface biomolecular combination (Fig. S7C).

3.2. Fabrication/characterization of PC interface-coated biochip

Our self-made PC interface-coated biochip is fabricated by a sequence of glass surface modifications (Fig. 2A). In particular, sufficient APTES is first exploited to actualize surface silanization for a well-cleaned cover glass. Then, the as-formed hydrophobic interface adheres to a thin layer of PDMS interface, followed by punching ten uniformly sized circular holes. After all these surface treatments, 240-nm CPSs dispersed droplets are added carefully to fill each hole and the final biochip is dried thoroughly at 37 °C to complete the deposition of CPSs. The aforementioned surface

transformation processes are directly observed by contact angle data (Fig. 2B). The tested angle reaches up to 134° when the water droplet is exposed to the PDMS interface. In contrast, it sharply decreases to less than 50° upon implementing the deposition event, uncovering a successful surface variation from a hydrophobic to a hydrophilic state. As expected, the deposited CPSs exhibit a characteristic self-assembly behavior and a highly-ordered periodic arrangement phenomenon is presented in the horizontal scanning

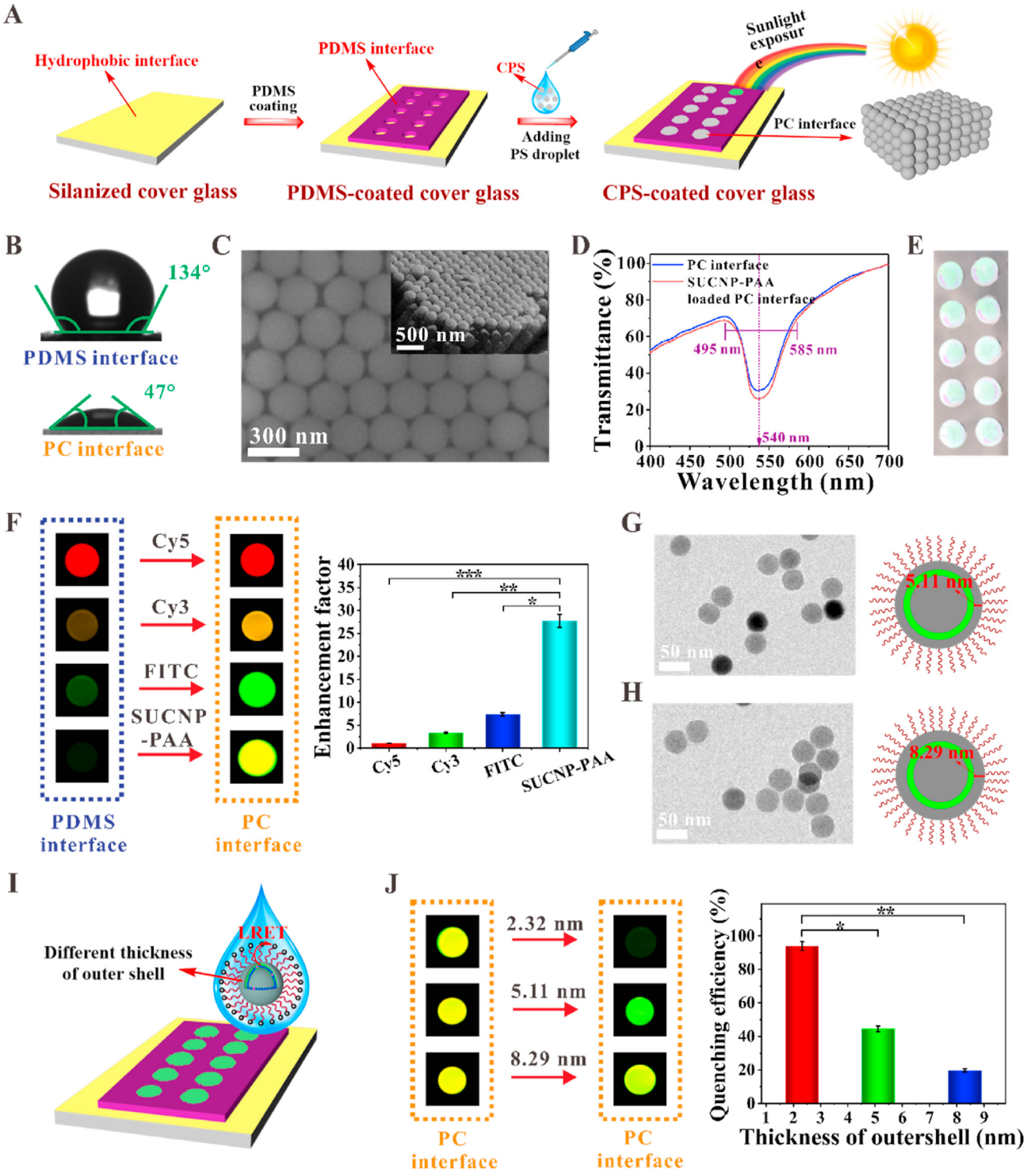

Fig. 2. (A) Fabrication steps of PC interface-coated biochip. (B) Contact angle data of PDMS and PC interfaces. (C) Horizontal SEM image (scale bar: 300 nm) of PC interface. Inset: cross-section SEM recording (scale bar: 500 nm). (D) Transmittance spectra of PC interface before and after loading with SUCNP-PAA. (E) Digital image of a representative biochip under sunlight exposure. (F) Left images: luminescence enhancement comparison between Cy5, Cy3, FITC and SUCNP-PAA on PDMS and PC interfaces. Right histograms: quantitative factors of these luminescent materials. Error bars represent three independent experiments. (G)–(H) TEM images of SUCNP-OA with thicker outer shells (5.11 nm and 8.29 nm). Scale bars are 50 nm. (I) Procedure of optimizing LRET efficiency on biochip. (J) Left images: LRET comparison between 2.32 nm, 5.11 nm and 8.29 nm of outer shells on PC interfaces. Right histograms: quantitative quenching efficiencies of these outer shell cases. Error bars represent three independent experiments. *P-value < 0.5, **P-value < 0.01.

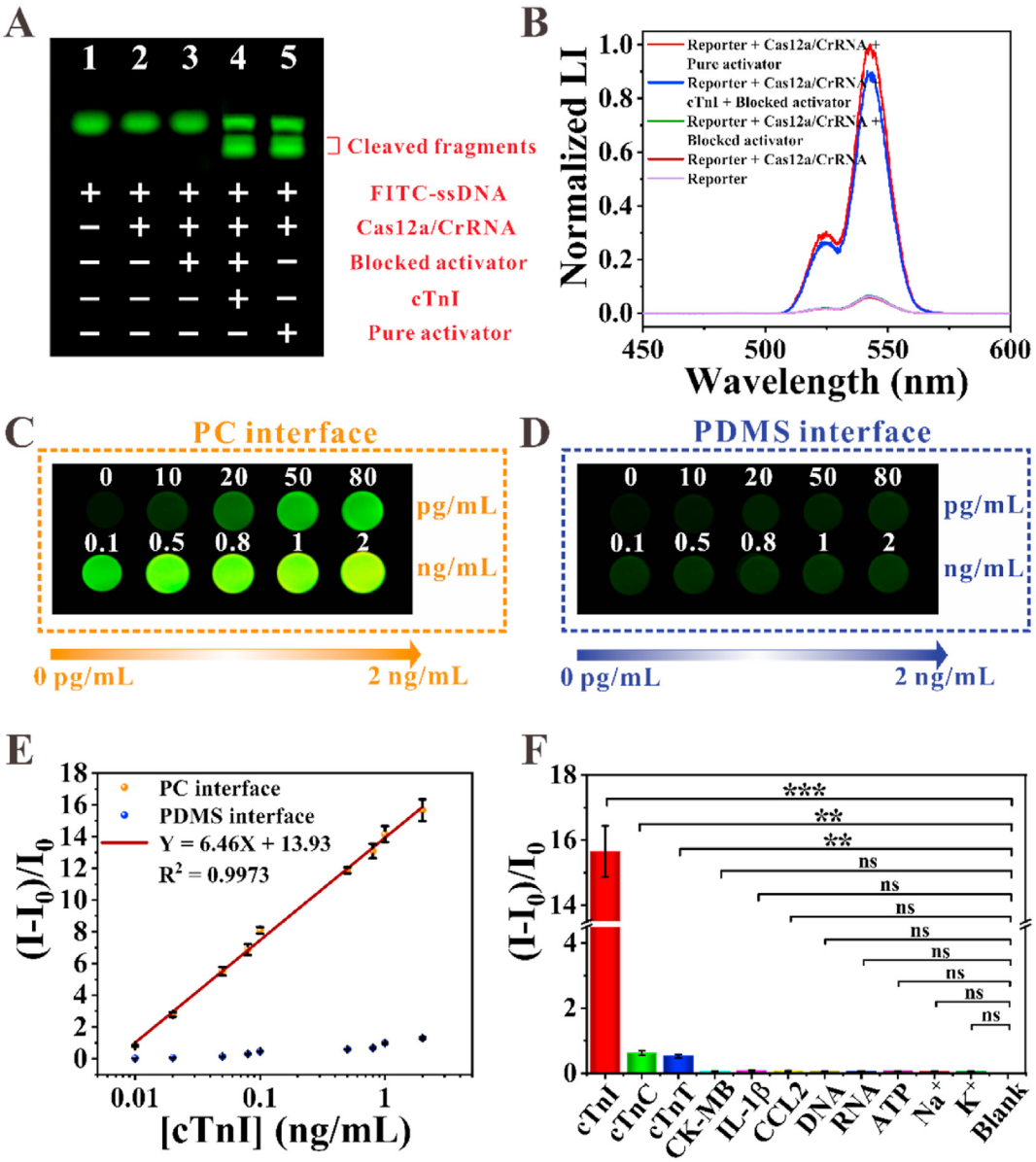

Fig. 3. (A) 6% PAGE experiment for examining the feasibility of dual-apatmer-regulated CRISPR/Cas12a system by *trans*-cleaving FITC-ssDNA. (B) Upconversion luminescence measurements of *trans*-cleavage on the surface of SUCNP-PAA. (C) Upconversion luminescence images of the CRISPR/Cas12a-powered biosensor by introducing with various amounts of cTnI (from 0 pg/mL to 2 ng/mL) on PC interface-coated biochip. (D) Upconversion luminescence images of this biosensor by introducing with various amounts of cTnI (from 0 pg/mL to 2 ng/mL) on PDMS interfaces. (E) Operational standard curve ($Y = 6.46X + 13.93$, R^2: 0.9973) between the concentration logarithm of cTnI (represented by "X") and the luminescence recovery ratio $[(I-I_0)/I_0$, represented by "Y"]. Orange and blue points indicate PC and PDMS interfaces, respectively. Error bars represent three independent experiments. (F) Inspection of assay specificity in the presence of cTnC, cTnT, CK-MB, IL-1β, CCL2, DNA, RNA, ATP, Na^+ and K^+. Concentrations of these substances are 5-fold higher than cTnI. Error bars represent three independent experiments. Ns: **P*-value > 0.5, **P*-value < 0.5, ***P*-value < 0.01, ****P*-value < 0.001. (For interpretation of the references to color in this figure legend, the reader is referred to the Web version of this article.)

electron microscopy (SEM) image (Fig. 2C). Notably, cross-section SEM recording (inset in Fig. 2C) demonstrates that such an assembling case owns a feature of multi-layer distributions and the thickness of this representative area is about 960 nm. The photonic bandgap of this array-type structure is further examined by transmittance spectra (blue line in Fig. 2D), from which the transmittance range is from 495 to 585 nm, and the most apparent gap point (the lowest transmission position) is concentrated at 540 nm. In addition, this intrinsic optical property will not be affected by the additional loading of SUCNP-PAA (red line in Fig. 2D). According to the principle of Bragg scattering, the PC coating manner endows a special photo-selective reflection effect, and the biochip presents an intense green brightness under the illumination of sunlight (Fig. 2E).

3.3. Investigating the enhancement of biochip towards upconversion luminescence

Two vital concerns must be paid close attention to before applying the dual-aptamer to regulate the CRISPR/Cas12a system. The first concern is whether the PC interface can promote upconversion luminescence, which is a prerequisite for sensitively conducting the subsequent imaging assay. To this end, three frequently used organic fluorescent dyes [cyanine 5 (Cy 5), cyanine 3 (Cy3), and fluorescein isothiocyanate (FITC)] and SUCNP-PAA are severally compared on the PC and PDMS interfaces under their

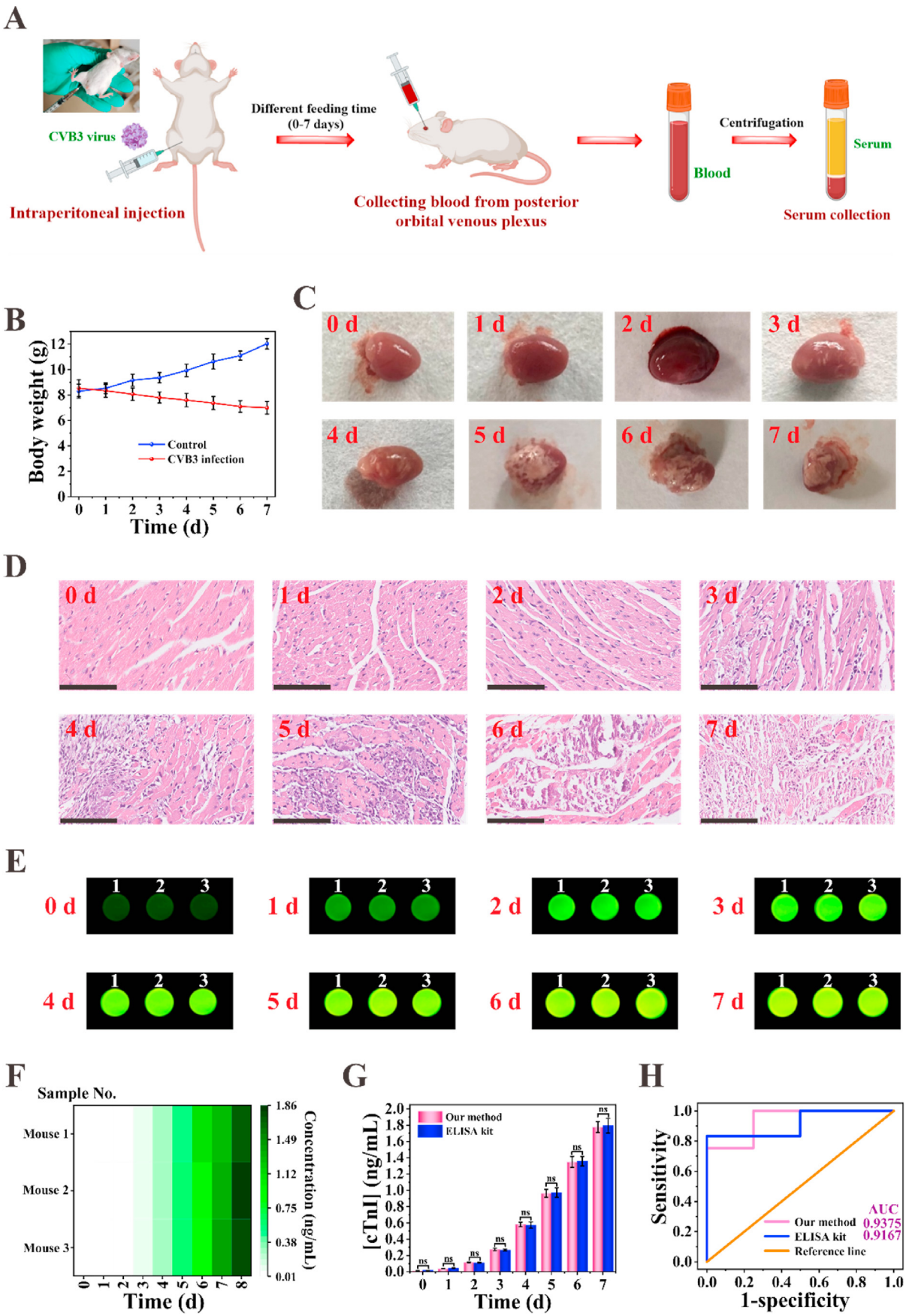
A
CVB3 virus
Intraperitoneal injection
Different feeding time
(0-7 days)
Collecting blood from posterior
orbital venous plexus
Blood
Centrifugation
Serum
Serum collection
B
Body weight (g)
Control
CVB3 infection
Time (d)
C
0 d
1 d
2 d
3 d
4 d
5 d
6 d
7 d
D
0 d
1 d
2 d
3 d
4 d
5 d
6 d
7 d
E
0 d
1 d
2 d
3 d
4 d
5 d
6 d
7 d
1 2 3
F
Sample No.
Mouse 1
Mouse 2
Mouse 3
Time (d)
Concentration (ng/mL)
1.86
1.49
1.12
0.75
0.38
0.01
G
Our method
ELISA kit
[cTnI] (ng/mL)
Time (d)
ns
H
Sensitivity
1-specificity
AUC
Our method 0.9375
ELISA kit 0.9167
Reference line

Fig. 4. (A) Construction procedures of viral myocarditis mouse model at different time points (0–7 days) and serum extraction steps. (B) Bodyweight variations in CVB3 virus infected mice and control mice. (C) Real heart anatomic images of CVB3 infected mice on different days. (D) H&E staining images of corresponding heart tissues. Scale bars are 100 μm. (E) Detection results of our method toward the mouse serums extracted from corresponding infection days. Three mice with similar body weights (RSD <10%) are measured for each testing day (white numbers). (F) Heat map of quantified serum cTnI contents *via* the linear relationship in Fig. 3E. (G) Comparison between our method and ELISA kit. Error bars represent three independent experiments. Ns: **P*-value > 0.5. (H) ROCs of our method (AUC value is 0.9375) and ELISA kit (AUC value is 0.9167).

corresponding optimal excitation sources. Given the best matching level between the photonic bandgap and the upconversion luminescence, SUCNP-PAA loading case has the most remarkable enhancement (left images in Fig. 2F). Further quantitative evaluations (right histograms in Fig. 2F) using the Image-J software illustrate a very high factor (~27-fold) attributed to this group. The data are observably reduced to 7.4 (FITC), 3.2 (Cy3), and 1.1 (Cy5). Besides this interesting result, negligible interfacial differences are present in the intra-batch and inter-batch of PC interfaces (Fig. S8). Overall, these solid foundations commendably guarantee that our self-made biochip can work as a potent effector for accomplishing signal amplification.

3.4. Optimizing the upconversion LRET efficiency on the biochip

Although an extremely restricted inner shell (2.17 nm) is successfully created to centralize the upconversion luminescence layer in the sandwich design, it is challenging to determine a suitable outer shell thickness that satisfies the proximity demand of LRET toward the pairing energy acceptors (surface BHQ-1). In response to this issue, thicker protection layers are tentatively synthesized based on the original core-shell structure. Following the Ostwald ripening chemistry (where the ligand numbers directly determine the particle size [42]), 5.11 nm (total diameter is 32.83 nm, Fig. 2H and S9A) and 8.29 nm of outer shells (total diameter is 36.01 nm, Fig. 2I and S9B) can be obtained by increasing the volume ratios of 1-ODE (1-octadecene)/OA (from 5:2 to 4:3 and 3:4). No variations in the crystal conformations (Fig. S10) and the ligand modifications (Fig. S11) occur in this size control. By converting these hydrophobic cases into corresponding water-soluble ones (Figs. S12 and S13) and further attaching with the reporters, the two complementary SUCNP-PAA based LRET models are studied on the biochip (Fig. 1G). The quenching effect becomes increasingly weak (left images in Fig. 2J) because the incremental outer shells will yield a longer LRET distance. Compared with the most conspicuous group (the outer shell is 2.32 nm and quenching efficiency is as high as 93.8%), the LRET capabilities are progressively decreased to 41.9% (5.11 nm) and 19.7% (8.29 nm), respectively, allowing an adjustable pathway for actualizing the energy-confined concept.

3.5. Evaluating the affinity of cTnI aptamer towards mouse source and examining the feasibility of dual-aptamer regulated CRISPR/Cas12a system

Because the currently discovered cTnI aptamer is mainly focused on applying human sources, whether it has a similar strong binding capability toward mouse source is crucial for achieving the proposed functional DNA regulation. For this purpose, agarose gel electrophoresis is first executed, where Fig. S14A that the aptamer incubated cTnI presents a distinctly shorter migration distance, implying that the aptamer can effectively identify the target. To further quantify the detailed affinity constant (defined as K_d), a simple magnetic sphere-assisted enzyme-linked immunosorbent assay (ELISA) is employed under different amounts of cTnI (Fig. S14B). The K_d is evaluated to be as low as ~174 pM (Figs. S14C and S14D), which is very comparable to that of human cTnI reported by Joe et al. (~270 pM) [45] and nearly one order of magnitude higher than that of the affinity of cTnI antibody.

Leveraging its high affinity, we examine the regulation feasibility of the dual-aptamer toward the CRISPR/Cas12a system by choosing a FITC labeled single-stranded DNA chain (termed as FITC-ssDNA) as the model cleavage substrate. As shown in the polyacrylamide electrophoresis (PAGE) experiment (Fig. 3A), no overt degradation phenomenon is observed for the absolutely blocked activator (lane 3), while a battery of short fragments appear upon introduction to the target (lane 4), demonstrating that the preferential recognition of the aptamers to cTnI can indeed release the activator to activate the CRISPR/Cas12a system. Such a *trans*-cleavage case is as efficient as a pure activator (lane 5). This finding is corroborated concurrently by transferring the cleavage reaction to the surface of SUCNP-PAA *via* the upconversion luminescence measurements (Fig. 3B), from which the highest luminescence recovery intensity (almost identical to the individual activation case) and an entirely silent manner are endowed with the aptamers regulation event and the inactive processing, respectively.

3.6. Assay performance towards standard mouse cTnI

On the strength of these preliminary findings, the assay performance in a standard mouse cTnI is being thoroughly examined after determining the optimal collateral cleavage conditions, among which the [Mg^{2+}], temperature, pH, and reaction time are set to 15 mM, 37 °C, 8.0 and 10 min, respectively, Fig. S15. Under different concentrations of cTnI (from 0 pg/mL to 2 ng/mL), the incremental target addition can make a more pronounced contribution to the signal recovery. Moreover, the brightness (false-color) of the round holes in our PC interface coated biochip is brightened inch by inch (Fig. 3C). In stark contrast (spanning the same concentration range), fairly weak hole brightness is collected on the PDMS interfaces because of the short luminescence amplification treatment. As a result, their signal intensities exhibit no obvious discriminations to the blank group (Fig. 3D). Furthermore, achieving the standard operational curve using the least squares principle confirms that the concentration logarithm of cTnI is strictly linear (R^2 is as high as 0.9973) to the luminescence recovery ratio [$(I-I_0)/I_0$, where I and I_0 denote the signal intensities in the presence and absence of targets, respectively] within two orders of magnitude. Of note, the RSD value of each point from three independent experiments is only ~5%, indicating that our biosensor has a stable optical signal output to ensure detection accuracy. Using the traditional criterion (three times the standard deviation of the blank signal divided by the slope of the linear equation) to calculate the limit of detection (LOD), the LOD of this newly raised CRISPR/Cas12a biosensor is down to 7.6 pg/mL. Such desirable sensitivity possesses an excellent superiority over the commercial ELISA kit (LOD = 100 pg/mL) and fierce competitiveness over other luminescence-based analytical methodologies (Table S1).

Except for the sensitivity inspection, specificity is another crucial assay indicator owing to the abundant interfering matrices in serum. To address this concern, two types of cTnI analogs such as cardiac troponin C (cTnC) and cardiac troponin T (cTnT), three other myocardial injury-associated proteins [creatine kinase-MB (CK-MB), interleukin-1β (IL-1β) and CCL2 chemokine (CCL2)], and five common biomolecules (DNA, RNA, ATP, Na^+, and K^+) are selected as the objects of determination. In Fig. 3F, aided by the excellent target identification affinity of the cTnI aptamer, the presence of these analogs can only slightly restore the quenched upconversion

luminescence (*P*-values < 0.01), even if their concentrations (5-fold) are visibly higher than that of the target group (2 ng/mL). Aside from this comparative result, on account of the improbable binding probabilities, the rest of the biological substances are hard to support implementing the expectant signal recovery manner. Their ratios reveal no considerable differences from the blank group (*P*-values > 0.5). Overall, our assay method has a commendable specificity for dealing with sensing requirements in complex samples.

3.7. Sensing cTnI in viral myocarditis mouse model

With assistance of the satisfactory assay performance, the intensively improved CRISPR/Cas12a-powered biosensor is finally employed to detect the content of cTnI in a carefully constructed viral myocarditis mouse model at different time points (from 0 to 7 days). Before this task, it is necessary to validate the underlying disturbances, including auto-luminescence and scattering light, for directly sensing such a challenging biological medium. Our sensing frame is further verified in whole serum to fulfill this goal, and the tiny variations in signal-to-background ratios indicate good working adaptation (Fig. S16). The definite construction procedures are displayed in Fig. 4A, wherein the CVB3 viruses in identical titers (10^2 $TCID_{50}$) are first injected intraperitoneally into a group of Balb/c mice (4-weeks-old-male) and housed in the same environments. Then, the corresponding whole blood from the posterior orbital venous plexus (RSD value of body weights is less than 10% for each testing group) is collected to extract the final yellow serums *via* centrifugation.

The monitoring of body weights (Fig. 4B) shows that the CVB3 virus-infected cases exhibited obvious decrease tendencies and an opposite phenomenon is found in the control mice. Successive anatomic images of the heart (Fig. 4C) uncover that the myocardial tissue injuries become increasingly severe with the evolution of feeding time, and such variation tendency is proven by the increasing degrees of inflammatory infiltrations in the hematoxylin-eosin (H&E) staining (Fig. 4D) and the dead cell labeling results (Fig. S17). Apart from this, the entire pathological process lasting for one week is confirmed explicitly by the echocardiographic recordings (Fig. S18). After utilizing our sensing method to quantitatively analyze the serum cTnI, it is observed that the detected signals represent a promotion sign and the RSD between three measured mice in each day is in a pretty narrow scope (Fig. 4E). Specific cTnI contents determined by the as-acquired linear standard curve is exhibited in the heat map (Fig. 4F), from which the average values (RSDs <15%) for different testing days are 12 pg/mL (0 days), 37 pg/mL (1 day), 116 pg/mL (2 days), 275 pg/mL (3 days), 581 pg/mL (4 days), 963 pg/mL (5 days), 1.349 ng/mL (6 days) and 1.776 ng/mL (7 dasy), and all the data are perfectly consistent with the assay results of clinically used ELISA kit (*P*-values > 0.5, Fig. 4G), showing a good sensing accuracy. Receiver operating characteristic curves (ROC) are applied to estimate the practical applicability of this detection strategy (Fig. 4H), and it is discovered that the obtained area under the curve (AUC, as high as 0.9375) is comparable to that of ELISA kit (AUC value is 0.9167), offering a promising dynamic disease tracer tool.

4. Conclusions

In this work, some rewarding sensing designs are introduced into a dual-aptamer regulated CRISPR/Cas12a system to promote its assay performance fully and successfully realize the dynamic monitoring of viral myocarditis injury in a CVB3 virus-infected mouse model. First, the upconversion LRET efficiency is significantly enhanced to 93.8% towards the surface attached BHQ-1 molecules by employing an exceptional energy-confined concept, wherein a sandwich-type UCNP is created *via* a thermal decomposition-based seed-growth preparation route and the luminescence domain can be adequately limited to approximately 2 nm of the inner shell. In addition, a nature-inspired PC interface-coated biochip is fabricated to implement upconversion luminescence enhancement, by which the detection signal is notably amplified to ~27-fold, owing to the best matching level of the photonic bandgap. After performing the collateral cleavage reaction on the surface of SUCNP-PAA and loading the products on the biochip, a convenient smartphone based imaging assay under a 980-nm portable laser device is conducted to the "off-to-on" luminescence output. These efforts markedly improve the sensing sensitivity to 7.6 pg/mL to determine cTnI with admirable specificity. Finally, the accurate sensing results toward mouse serum samples demonstrated that the proposed is able to accurately trace the specific myocardial injuries during the complete pathological process, endowing a prospective diagnostic platform.

CRediT authorship contribution statement

Li-Li Lu: Conceptualization, Methodology, Validation, Investigation, Funding acquisition. **Chao-Zhi Li:** Validation, Investigation, **Yu-Heng Liu:** Validation, Investigation. **Heng-Zhong Guo:** Validation, Investigation. **Da Liu:** Validation, Investigation. **Hong-Wu Tang:** Funding acquisition. **Bei Zheng:** Validation, Investigation. **Cheng-Yu Li:** Conceptualization, Methodology, Validation, Investigation, Writing – original draft, Writing – review & editing, Visualization, Supervision, Project administration, Funding acquisition.

Declaration of competing interest

The authors declare that they have no known competing financial interests or personal relationships that could have appeared to influence the work reported in this paper.

Acknowledgments

This work was supported by the National Natural Science Foundation of China (21904102, 81700446, 21827808 and 81772256) and we gratefully thanked Prof. Kailang Wu of Wuhan University for offering us the CVB3 virus.

Appendix A. Supplementary data

Supplementary data to this article can be found online at https://doi.org/10.1016/j.aca.2022.339455.

References

[1] N. Lasrado, J. Reddy, An overview of the immune mechanisms of viral myocarditis, Rev. Med. Virol. 30 (6) (2020), e2131.
[2] M. Olejniczak, M. Schwartz, E. Webber, A. Shaffer, T.E. Perry, Viral myocarditis-incidence, diagnosis and management, J. Cardiothorac. Vasc. Anesth. 34 (6) (2020) 1591–1601.
[3] X. Wei, Y. Fang, H.D. Hu, Consideration on pathogen of viral fulminant myocarditis, Eur. Heart J. 41 (22) (2020), 2120-2120.
[4] S. Negrotto, C.J. de Giusti, L. Rivadeneyra, A.E. Ure, H.A. Mena, M. Schattner, R.M. Gomez, Platelets interact with Coxsackieviruses B and have a critical role in the pathogenesis of virus-induced myocarditis, J. Thromb. Haemostasis 13 (2) (2015) 271–282.
[5] S. Yuen, J. Smith, L. Caruso, M. Balan, M.A. Opavsky, The coxsackie-adenovirus receptor induces an inflammatory cardiomyopathy independent of viral infection, J. Mol. Cell. Cardiol. 50 (5) (2011) 826–840.

[6] Y. Kurland, R.I. Kylat, D.C. Johnson, B.J. Barber, A.D. Bedrickt, M.Y. Bader, Intravenous immunoglobulin for congenital parvovirus myocarditis, J Pediat Inf Dis-Ger 15 (1) (2020) 53–56.

[7] R. Ozdemir, M. Kucuk, S.E. Dibeklioglu, Report of a myocarditis outbreak among pediatric patients: human herpesvirus 7 as a causative agent? J. Trop. Pediatr. 64 (6) (2018) 468–471.

[8] S.P. Murphy, M.F. Prescott, A.S. Maisel, J. Butler, I.L. Pina, G.M. Felker, J.H. Ward, K.M. Williamson, A. Camacho, R.R. Kandanelly, S.D. Solomon, J.L. Januzzi, Association between angiotensin receptor-neprilysin inhibition, cardiovascular biomarkers, and cardiac remodeling in heart failure with reduced ejection fraction, Circ-Heart Fail 14 (6) (2021), e008410.

[9] A. Clerico, A. Aimo, M. Cantinotti, Cardiac biomarkers for outcome prediction in infant bronchiolitis: too soon to discard troponin? Clin. Chim. Acta 518 (2021) 170–172.

[10] A. Hussain, O. Tang, C. Sun, X.M. Jia, E. Selvin, V. Nambi, A. Folsom, G. Heiss, F. Zannad, T. Mosley, S.S. Virani, J. Coresh, E. Boerwinkle, B. Yu, J.W. Cunningham, A.M. Shah, S.D. Solomon, J.A. de Lemos, R.C. Hoogeveen, C.M. Ballantyne, Soluble angiotensin-converting enzyme 2, cardiac biomarkers, structure, and function, and cardiovascular events (from the atherosclerosis risk in communities study), Am. J. Cardiol. 146 (2021) 15–21.

[11] X.Y. Guo, L.J. Zong, Y.C. Jiao, Y.F. Han, X.P. Zhang, J. Xu, L. Li, C.W. Zhang, Z.P. Liu, Q. Ju, J.H. Liu, Z.H. Xu, H.D. Yu, W. Huang, Signal-enhanced detection of multiplexed cardiac biomarkers by a paper-based fluorogenic immunodevice integrated with zinc oxide nanowires, Anal. Chem. 91 (14) (2019) 9300–9307.

[12] K.W. Lee, K.R. Kim, H.J. Chun, K.Y. Jeong, D.K. Hong, K.N. Lee, H.C. Yoon, Time-resolved fluorescence resonance energy transfer-based lateral flow immunoassay using a raspberry-type europium particle and a single membrane for the detection of cardiac troponin I, Biosens. Bioelectron. 163 (2020) 112284.

[13] W.Y. Lim, T.M. Thevarajah, B.T. Goh, S.M. Khor, Paper microfluidic device for early diagnosis and prognosis of acute myocardial infarction via quantitative multiplex cardiac biomarker detection, Biosens. Bioelectron. 128 (2019) 176–185.

[14] Y. Song, X.L. Cai, G. Ostermeyer, J.R. Yu, D. Du, Y.H. Lin, Self-assembling allochroic nanocatalyst for improving nanozyme-based immunochromatographic assays, ACS Sens. 6 (1) (2021) 220–228.

[15] N.A. Schneck, K.W. Phinney, S.B. Lee, M.S. Lowenthal, Quantification of cardiac troponin I in human plasma by immunoaffinity enrichment and targeted mass spectrometry, Anal. Bioanal. Chem. 410 (11) (2018) 2805–2813.

[16] Y.F. Dong, X.L. Qin, M.H. Wang, C.Y. Gu, Z.W. Zhu, D. Yang, Y.H. Shao, Electrochemiluminescent detection of proteins based on fullerenols modified gold nanoparticles and triple amplification approaches, Anal. Chem. 92 (2) (2020) 1890–1897.

[17] D.X. Du, J.N. Shu, M.Q. Guo, M.A. Haghighatbin, D. Yang, Z.P. Bian, H. Cui, Potential-Resolved differential electrochemiluminescence immunosensor for cardiac troponin I based on MOF-5-wrapped CdS quantum dot nanoluminophores, Anal. Chem. 92 (20) (2020) 14113–14121.

[18] X.N. Mi, H. Li, R. Tan, Y.F. Tu, Dual-modular aptasensor for detection of cardiac troponin I based on mesoporous silica films by electrochemiluminescence/electrochemical impedance spectroscopy, Anal. Chem. 92 (21) (2020) 14640–14647.

[19] C.Y. Li, B. Zheng, J.T. Li, J.L. Gao, Y.H. Liu, D.W. Pang, H.W. Tang, Holographic optical tweezers and boosting upconversion luminescent resonance energy transfer combined clustered regularly interspaced short palindromic repeats (CRISPR)/Cas12a biosensors, ACS Nano 15 (5) (2021) 8142–8154.

[20] H.X. Gong, Y.L. Wu, R.J. Zeng, Y.Y. Zeng, X.L. Liu, D.A.P. Tang, CRISPR/Cas12a-mediated liposome-amplified strategy for the photoelectrochemical detection of nucleic acid, Chem. Commun. 57 (71) (2021) 8977–8980.

[21] C.Y. Li, B. Zheng, L.L. Lu, W.K. Fang, M.Q. Zheng, J.L. Gao, Y.H. Liu, D.W. Pang, H.W. Tang, Biomimetic chip enhanced time-gated luminescent CRISPR-cas12a biosensors under functional DNA regulation, Anal. Chem. 93 (37) (2021) 12514–12523.

[22] J.S. Chen, E.B. Ma, L.B. Harrington, M. Da Costa, X.R. Tian, J.M. Palefsky, J.A. Doudna, CRISPR-Cas12a target binding unleashes indiscriminate single-stranded DNase activity, Science 360 (6387) (2018) 436–439.

[23] J.S. Gootenberg, O.O. Abudayyeh, M.J. Kellner, J. Joung, J.J. Collins, F. Zhang, Multiplexed and portable nucleic acid detection platform with Cas13, Cas12a, and Csm6, Science 360 (6387) (2018) 439–444.

[24] J.L. Gao, Y.H. Liu, J.X. Liu, H.W. Tang, C.Y. Li, A photoresponsive and metal-organic framework encapsulated DNA tetrahedral entropy-driven amplifier for high-performance imaging intracellular MicroRNA, Anal. Chem. 93 (39) (2021) 16638–16645.

[25] Z.C. Yu, H.X. Gong, Y.X. Li, J.H. Xu, J. Zhang, Y.Y. Zeng, X.L. Liu, D.P. Tang, Chemiluminescence-derived self-powered photoelectrochemical immunoassay for detecting a low-abundance disease-related protein, Anal. Chem. 93 (39) (2021) 13389–13397.

[26] Z.P. Yin, L. Zhu, Z.J. Lv, M.J. Li, D.A.P. Tang, Persistent luminescence nanorods-based autofluorescence-free biosensor for prostate-specific antigen detection, Talanta 233 (2021), 122563.

[27] Z.M. Zhang, S. Shikha, J.L. Liu, J. Zhang, Q.S. Mei, Y. Zhang, Upconversion nanoprobes: recent advances in sensing applications, Anal. Chem. 91 (1) (2019) 548–568.

[28] Z.B. Luo, Q.G. Qi, L.J. Zhang, R.J. Zeng, L.S. Su, D.P. Tang, Branched polyethylenimine-modified upconversion nanohybrid-mediated photoelectrochemical immunoassay with synergistic effect of dual-purpose copper ions, Anal. Chem. 91 (6) (2019) 4149–4156.

[29] Z.B. Luo, L.J. Zhang, R.J. Zeng, L.S. Su, D.P. Tang, Near-infrared light-excited core-core-shell UCNP@Au@CdS upconversion nanospheres for ultrasensitive photoelectrochemical enzyme immunoassay, Anal. Chem. 90 (15) (2018) 9568–9575.

[30] Z.L. Qiu, J. Shu, D.P. Tang, Near-Infrared-to-Ultraviolet light-mediated photoelectrochemical aptasensing platform for cancer biomarker based on core shell NaYF4:Yb,Tm@TiO2 upconversion microrods, Anal. Chem. 90 (1) (2018) 1021–1028.

[31] Z.L. Qiu, J. Shu, J.F. Liu, D.P. Tang, Dual-channel photoelectrochemical ratiometric aptasensor with up-converting nanocrystals using spatial-resolved technique on homemade 3D printed device, Anal. Chem. 91 (2) (2019) 1260–1268.

[32] G. Wang, Y.K. Fu, Z.H. Ren, J. Huang, S. Best, X. Li, G.R. Han, Upconversion nanocrystal "armoured' silica fibres with superior photoluminescence for miRNA detection, Chem. Commun. 54 (49) (2018) 6324–6327.

[33] M.P. Gao, R.Y. Wu, Q.S. Mei, C.L. Zhang, X. Ling, S.S. Deng, H.B. He, Y. Zhang, Upconversional nanoprobes with highly efficient energy transfer for ultrasensitive detection of alkaline phosphatase, ACS Sens. 4 (11) (2019) 2864–2868.

[34] Y.J. Zhao, Z.Y. Xie, H.C. Gu, C. Zhu, Z.Z. Gu, Bio-inspired variable structural color materials, Chem. Soc. Rev. 41 (8) (2012) 3297–3317.

[35] R.A. Potyrailo, R.K. Bonam, J.G. Hartley, T.A. Starkey, P. Vukusic, M. Vasudev, T. Bunning, R.R. Naik, Z.X. Tang, M.A. Palacios, M. Larsen, L.A. Le Tarte, J.C. Grande, S. Zhong, T. Deng, Towards outperforming conventional sensor arrays with fabricated individual photonic vapour sensors inspired by Morpho butterflies, Nat. Commun. 6 (2015) 7959.

[36] Q. Yao, Y.Q. Wang, J. Wang, S.M. Chen, H.Y. Liu, Z.R. Jiang, X.E. Zhang, S.M. Liu, Q. Yuan, X. Zhou, An ultrasensitive diagnostic biochip based on biomimetic periodic nanostructure-assisted rolling circle amplification, ACS Nano 12 (7) (2018) 6777–6783.

[37] Y.Q. Wang, Z.H. Li, Q.S. Lin, Y.R. Wei, J. Wang, Y.X. Li, R.H. Yang, Q. Yuan, Highly sensitive detection of bladder cancer-related miRNA in urine using time-gated luminescent biochip, ACS Sens. 4 (8) (2019) 2124–2130.

[38] Q. Li, S.H. Zhou, T. Zhang, B. Zheng, H.W. Tang, Bioinspired sensor chip for detection of miRNA-21 based on photonic crystals assisted cyclic enzymatic amplification method, Biosens. Bioelectron. 150 (2020), 111866.

[39] R.C. Castro, J.X. Soares, D.S.M. Ribeiro, J.L.M. Santos, Dual-emission ratiometric probe combining carbon dots and CdTe quantum dots for fluorometric and visual determination of H2O2, Sensor. Actuator. B Chem. 296 (2019), 126665.

[40] R.C. Castro, D.S.M. Ribeiro, J.L.M. Santos, Visual detection using quantum dots sensing platforms, Coord. Chem. Rev. 429 (2021), 213637.

[41] R.C. Castro, R.N.M.J. Pascoa, M.L.M.F.S. Saraviva, J.L.M. Santos, D.S.M. Ribeiro, Photoluminescent and visual determination of ibandronic acid using a carbon dots/AgInS2 quantum dots ratiometric sensing platform, Spectrochim. Acta 267 (2022), 120592.

[42] H. Guo, Z.Q. Li, H.S. Qian, Y. Hu, I.N. Muhammad, Seed-mediated synthesis of NaYF4:Yb, Er/NaGdF4 nanocrystals with improved upconversion fluorescence and MR relaxivity, Nanotechnology 21 (12) (2010), 125602.

[43] I. Hyppanen, N. Hoysniemi, R. Arppe, M. Schaferling, T. Soukka, Environmental impact on the excitation path of the red upconversion emission of nanocrystalline NaYF4:Yb3+,Er3+, J. Phys. Chem. C 121 (12) (2017) 6924–6929.

[44] V. Gabelica, F. Rosu, T. Tabarin, C. Kinet, R. Antoine, M. Broyer, E. De Pauw, P. Dugourd, Base-dependent electron photodetachment from negatively charged DNA strands upon 260-nm laser irradiation, J. Am. Chem. Soc. 129 (15) (2007) 4706–4713.

[45] H. Jo, H. Gu, W. Jeon, H. Youn, J. Her, S.K. Kim, J. Lee, J.H. Shin, C. Ban, Electrochemical aptasensor of cardiac troponin I for the early diagnosis of acute myocardial infarction, Anal. Chem. 87 (19) (2015) 9869–9875.